BULLETIN OF THE POLISH ACADEMY OF SCIENCES TECHNICAL SCIENCES, Vol. 73(6), 2025, Article number: e155047 DOI: 10.24425/bpasts.2025.155047

MECHANICAL AND AERONAUTICAL ENGINEERING, THERMODYNAMICS

# Studies of energy absorption of lattice structures manufactured from PETG filament with FFF 3D printing

Mateusz BANASZEK<sup>1</sup>, Paweł BARANOWSKI<sup>1</sup>, Paweł PŁATEK<sup>2</sup>, Marcin SARZYŃSKI<sup>2</sup>, and Kamil CIEPLAK<sup>2</sup>

Abstract. This paper presents experimental and numerical results of the mechanical response of body-centered cubic (BCC) lattice structures manufactured with the fused filament fabrication (FFF) method using polyethylene terephthalate glycol (PETG) material. The BCC structures were subjected to uniaxial compression tests using a universal strength machine with three different values of deformation velocities. Moreover, dog-bone specimens were manufactured in three orientations to identify the PETG mechanical properties, which were supplemented with the literature data of PETG tested under compression. Then, the mechanical properties were correlated in the LS-Dyna code using a visco-plastic material model, which was used to numerically reproduce the experimental uniaxial tensile test conditions. The compression tests of BCC were simulated, and the results of experiments and numerical simulations were compared with satisfactory agreement. It was demonstrated that the properties of the 3D printed PETG varied, depending on both the printing direction and the type of applied load condition (compression/tension). Furthermore, the results also show that for the strut-based lattice structures manufactured with the FFF method and PETG material, it is mandatory to consider the above remark while simulating this type of mechanical behavior in a structure. Additionally, the influence of element type and cross section of the struts was also analyzed in this work. Results presented in the paper confirmed that the BCC lattice structures were effective in terms of energy absorption capacity, and they demonstrated long-range plateau deformation force plots.

Keywords: truss-based lattice; BCC; 3D printing; PETG; fused filament fabrication; additive manufacturing.

#### 1. INTRODUCTION

Cellular structural materials attract the interest of many scientists due to their unique physical and mechanical properties. They exist in nature, and their distinctive characteristics have often attracted attention and inspired scientists and engineers, particularly because of their low relative density and specific mechanical properties. Their ability to provide high structural stiffness or absorption of mechanical energy through deformation makes them particularly attractive for engineering applications [1–9]. However, a production of such materials has been either impossible or significantly restricted due to technological limitations [10, 11]. The emergence and growing popularity of additive manufacturing (AM) techniques have accelerated considerable research on the design, production, and analysis of mechanical properties of regular cellular structures [12, 13]. These production methods are applied in many branches of industry: aerospace, automotive, defense, civil engineering, and bioengineering, as well as in medicine and art, enabling the

Manuscript submitted 2025-03-16, revised 2025-08-06, initially accepted for publication 2025-08-08, published in November 2025.

production of objects with diverse mechanical properties and varying sizes [12–16]. Depending on the geometry and size of the unit cell, the cellular structures can be classified into two main categories: 2D and 3D.

2D structures are the subject of research in numerous numerical-experimental studies [17]. The primary objective of these studies was to evaluate the mechanical response of structures that differ in the unit cell (shape and dimensions), considering various types of mechanical loading (tension, compression, bending) and taking into account the effect of strain rate (quasi-static, dynamic, and impact tests) [18, 19]. The number of studies on 3D cellular structures is currently lower compared to 2D variants. This difference arises from the fact that their manufacturing process is more complex. However, their significantly lower relative density makes them attractive to many industrial sectors. The 3D cellular structured materials are most commonly classified into four main groups of lattices: trussbased, plate-based, shell-based, and hierarchical [11, 20, 21]. The first are the most widely used due to their beam-like architecture [2, 5, 21–25]. These structures exhibit excellent energy absorption (EA) capabilities and controlled deformation. The extent of the plateau region varies depending on the used material [1,2,4,5]. Among 3D lattice structures, four primary types of elementary cells can be distinguished: body-centered cubic

<sup>&</sup>lt;sup>1</sup> Military University of Technology, Faculty of Mechanical Engineering, Institute of Mechanics and Computational Engineering, ul. Gen. S. Kaliskiego 2, 00-908 Warsaw, Poland

<sup>&</sup>lt;sup>2</sup> Military University of Technology, Faculty of Mechatronics, Armament and Aerospace, Institute of Armament Technique, ul. Gen. S. Kaliskiego 2, 00-908 Warsaw, Poland

<sup>\*</sup>e-mail: mateusz.banaszek@student.wat.edu.pl

(BCC), body-centered cubic with Z-strut (BCCZ), face-centered cubic (FCC), and face-centered cubic with Z-strut (FCCZ) [11].

A lot of research focuses on the EA characteristics of metallic 3D cellular structures [1, 4–6, 23, 26]. Li et al. [2] investigated BCC structures fabricated using selective laser melting (SLM) with 316L stainless steel. Their study involved uniaxial compression tests, from which stress-strain curves were obtained and subsequently validated through numerical simulations. In [5], the BCC structures were also subjected to uniaxial compression tests, with additional investigation into the effect of the heating temperature on the resulting stress-strain curves. Beyond conventional BCC structures, Seharing et al. [26] explored the influence of elementary cell gradients on EA properties. In their study, the relative density of individual cells varied along different heights of the structure. An interesting analysis was presented in [23], where the authors examined the impact of cross-sectional variations in individual beams on the structural strength of AlSi10Mg lattice structures. Their findings indicated that the stress concentration from the center of the elementary cell to the center of the beam significantly affected the mechanical response.

In addition to static tests, lattice structures are also subjected to dynamic loading conditions [4, 6]. The authors of [6] compared the EA capacity of 2D and 3D chiral structures. Smith et al. [4] investigated the behavior of BCC and BCCZ structures fabricated via SLM using 316L stainless steel under detonation conditions, highlighting differences in their response to extreme dynamic loads. It was shown that EA at the front of a structure varied depending on its relative density. Maconachie et al. [1] conducted a comprehensive review of 3D lattice structures fabricated using selective laser melting (SLM). Their study outlined best practices and consolidated experimental data from literature. Compared to metal-based lattices, fewer studies focus on 3D lattice structures made from plastics. The earliest materials used in this context include ABS and PLA [3, 9, 27]. Seek et al. [27] compared the EA properties of simple cubic (SC), honeycomb (HC), BCC, and PeckGy80 (PG80) structures fabricated from PLA. Their study demonstrated that altering the elementary cell type significantly affected the resulting forcedisplacement curves. In [3], the effect of increasing the number of elementary cells in BCC trusses and modifying the cross section of the sub-elementary beams was investigated. Specimens were fabricated using the SLA technique and compared with numerical simulations. The findings revealed that structures with a higher number of elementary cells and smaller beam cross sections exhibited superior EA compared to those with fewer cells and larger beam cross sections. Studies on PETG-based lattice structures are less common [9,22,28-30]. Natesan et al. [29] examined Schwarz P-type triply periodic minimal surface (TPMS) structures, comparing different elementary cell sizes to assess their impact on EA capabilities. In [28], the authors evaluated the performance of foam-filled 3D lattice structures.

Specific features of lattice structures inspire their investigation not only in compression but also under tension loading conditions. Researchers in [22] compare the mechanical properties of polylactic acid (PLA), acrylonitrile butadiene styrene (ABS), and polyethylene terephthalate glycol (PETG) across different

lattice structures in cross section geometry. Their results indicated that the truss configuration plays a crucial role in tensile loading scenarios, highlighting its major influence on structural performance.

The present study is focused on the BCC truss-based lattice variant, which was thoroughly studied in previous papers [1–3, 11, 21–23]. However, the most frequently utilized technique is the PBF (powder bed fusion) AM, while there is a limited number of studies in which the FFF method and PETG were incorporated in the production of 3D lattice structures, especially BCC. To highlight this research gap, the present paper expands a current knowledge in this area and demonstrates the following original aspects: (1) implementation of both experimental and numerical studies related to the mechanical response of truss-based lattice structures made additively via FFF from PETG filament under quasi-static compression tests, (2) demonstration of a direct influence of the printing orientation and strong anisotropy on the mechanical response of FFF PETG material, (3) a comprehensive correlation and validation of the elasto-viscoplastic constitutive model based on different loading conditions (tension/compression) and printing orientation.

Experimental tests were preceded by additional technological attempts to identify the most efficient 3D printing parameters. Tensile dog-bone specimens were manufactured according to ASTM D638-14 standard to determine the mechanical properties of PETG filaments, as well as to verify the influence of the 3D printing direction. The data of the obtained material were supplemented by the compression properties taken from the relevant literature [31]. Based on the gathered data, computer simulations were performed using the FEA approach implemented in the LS-Dyna software. A strong anisotropy observed during the experimental tests led to the adoption of an appropriate approach in the utilized constitutive model. Unfortunately, there are no such material models available in the LS-Dyna software that allow for the definition of the mechanical properties of materials 3D printed via the FFF technique belonging to the material extrusion (MEx) group. Therefore, in the present paper, direct implementation of the stress vs. strain curves in the selected elasto-viscoplastic model was considered. The obtained results allow for additional parametric studies directed to analyze the potential application of developed lattice structures in engineering applications. The results demonstrate that in the case of lattice structures produced by the FFF method [15, 32] from PETG filament, it is not possible to rely only on tensile testing of specimens produced in one orientation. Furthermore, brick elements were found to be more efficient in reproducing the behavior of the simulated BCC topology compared to the 1D representation.

#### 2. CHARACTERIZATION OF BCC LATTICES

## 2.1. Geometrical assumption of the tested BCC lattice structures

The BCC topology manufactured from PETG material was studied under compression loading conditions. Both experimental and numerical studies were considered with the hexago-

nal cross sections of the struts. Moreover, two additional struts cross section variants (i.e., square and round) were investigated, using a computer simulation approach. The designed BCC structures had a cubical shape with a total dimension of  $\sim 85.0 \times 85.0 \times 85.0$  mm and a relative density value close to 0.07. The relative density is expressed by the equation

$$\rho_{\rm rel} = \frac{\rho^*}{\rho_s} \,, \tag{1}$$

where  $\rho^*$  – density of structure,  $\rho_s$  – density of solid material.

Five unit cells across the width/height/length with a dimension of  $\sim 17.0$  mm were assumed during the design process. The cross-sectional area for all tested variants of the strut was kept at the same value. Additional structure variants were proposed to analyze the influence of the FFF 3D printing technique on the obtained results since a significant discrepancy between the computer simulation results and data gathered from the experimental tests was observed (see Section 5.3). It was assumed that the differences between FEA and experimental outcomes could be justified by the applied 3D printing direction and strut dimensions, which were different in the BCC topologies compared to the dog-bone specimens used for the uniaxial testing. Therefore, two types of cubical specimens were manufactured with dimensions close to four elementary cells of the BCC structure, i.e.,  $34.0 \times 34.0 \times 34.0$  mm, named BCC\_s (small) and SQ (square). For each variant, three specimens were prepared and subjected to uniaxial compression tests. Obtained outcomes enable evaluation of whether there is a relation between 3D printing direction and the mechanical response of manufactured specimens.

The geometrical representations of all lattice structures considered in this work, with the presented dimensions, is shown in Fig. 1.

## 2.2. Characterization of the applied FFF 3D printing process

To manufacture the BCC lattice structures and dog-bone specimens for material testing, the commercial PETG filament was used; its basic properties are shown in Table 1. The Prusa i3 MK3S 3D printer was used, and the parameters for the 3D printing process are shown in Table 2. Many filament producers declare other mechanical properties of PETG, which pose an additional challenge in the process of defining mechanical parameters [33–36]. Thus, to minimize the impact of incorrectly defined PETG material parameters, twelve dog-bone specimens were manufactured. Moreover, nine BCC topologies were also manufactured (Fig. 2). Furthermore, the geometrical properties of dog-bone specimens are also included (details regarding the specimens for material testing are provided in Section 3.1). In Fig. 3, additional printed cubical specimens are also shown, with visible different 3D printing directions. Thus, in the compression tests, the material itself was assessed under different loading conditions to analyze the influence of building orientation on the obtained results, since significant discrepancies between the numerical results and experimental tests were observed while compressing the BCC lattice structures.

**Table 1**Mechanical properties of PETG [35]

Constant	Value	Unit
Density, $\rho$	1270.0	kg/m <sup>3</sup>
Elastic modulus E	1800.0	MPa
Poisson's ratio, v	0.39	-
Yield stress, $R_e$	42.0	MPa

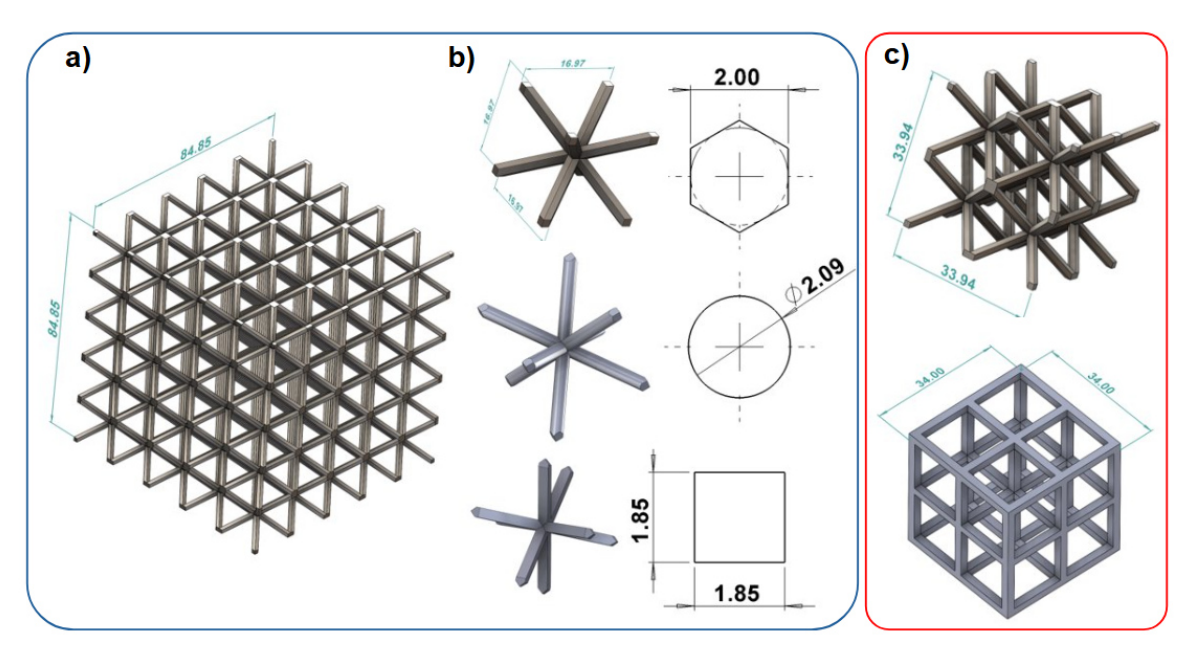


Fig. 1. a) A general 3D view of BCC lattice structure, b) strut cross sections, c) cubical specimens

**Table 2**3D printing parameters for specimen fabrication

Process parameter	Value		
Nozzle diameter	0.6 mm		
Layer height	0.3 mm		
Fill density	100%		
	45.0 mm/s for contour		
Printing speed	35.0 mm/s for small contour		
	55.0 mm/s for filling		
Extrusion width	0.65 mm		
Nozzle temperature	240°C		
Bed temperature	90°C		
Number of contour lines	2		
Cooling	On		
Sequence printing	On		

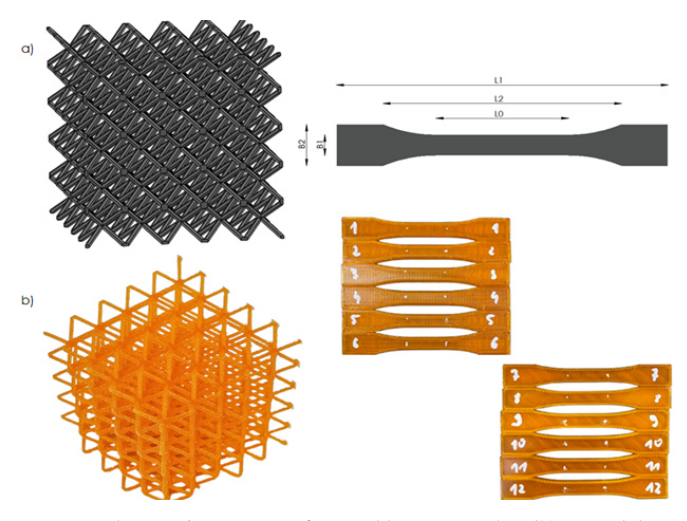


Fig. 2. The specimens manufactured by FFF: a) 3D CAD models, b) printed specimens

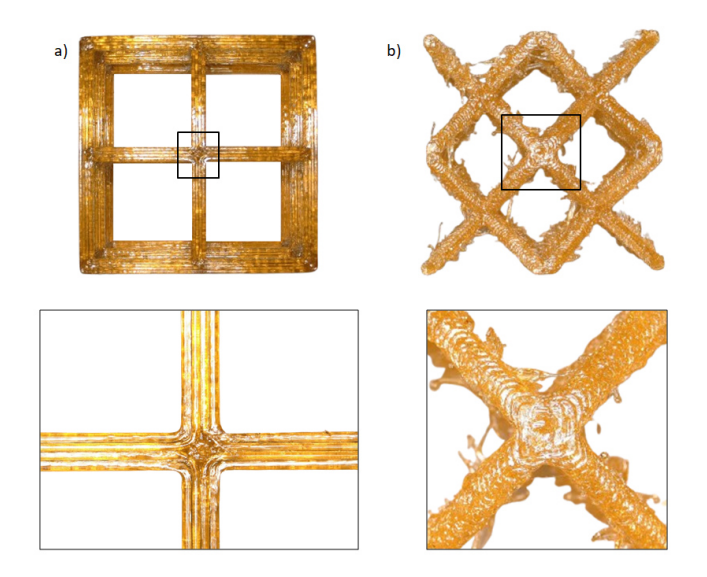


Fig. 3. The specimens manufactured by FFF: a) cubic, b) BCC lattice

#### 2.3. Quality evaluation of the manufactured specimens

Before performing experimental tests with the use of BCC lattice structures and dog-bone specimens, the quality control of the fabricated specimens was conducted. Based on the digital microscopy images (Fig. 4), it was possible to verify the geometrical dimensions of the specimens by comparing them with the designed BCC topologies. The quality analysis was conducted using the Keyence VHX 6000 digital microscope with dedicated software. The quality of the struts and the porosity level were analyzed. A detailed measurement of the struts showed that the strut thickness (diameter) varied and was not equal to the geometrical model at each of the given measurement points. The discrepancies between the actual and CAD models vary between 0.1 mm and 0.15 mm. Based on the measurements, the numerical models were prepared considering the above dimensions of the struts.

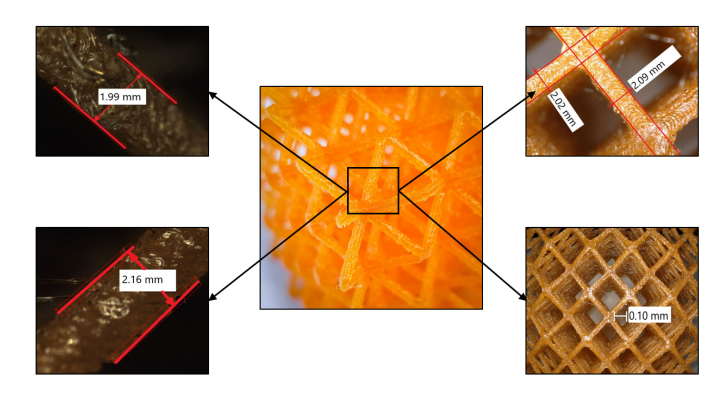


Fig. 4. Evaluation of lattice strut using optical microscope

#### 3. PETG MATERIAL PROPERTIES

#### 3.1. Material data acquisition

In general, the uniaxial tensile test seems to be a relatively simple and basic method used to obtain the required material data. However, in the case of PETG, several scholars highlighted that this specific filament is quite problematic to perform tests via tension [37-39] or compression. For example, in [37] it was shown that the speed and temperature of specimens printing process affected their strength. On the other hand, in [38], the authors demonstrated that the shape of specimens and orientation of printed layers impacted the mechanical properties of PETG. Moreover, Ergene et al. [39] studied the effect of tensile test speed and layer thickness on PETG parameters, while in [31, 40], the authors verified the mechanical properties of PETG in compression tests. It is worth noticing that various producers of PETG filament also declare different mechanical properties [33–36]. In the previous papers [8, 37–39, 41, 42], it was also proven that the mechanical properties of 3D printed materials strongly depended on the printing parameters. Therefore, the material parameters of the PETG filament were verified in three printing directions: X (T1), at an angle of 45° (T2), and Z (T3). The uniaxial tensile tests were conducted for the specimens prepared according to ASTM D638-14 standard [43].

Furthermore, the literature data for the compressive loading of PETG were also included [31], which were named as: C1, C2, and C3 for the Z, X, and Y printing directions, respectively. Based on the obtained results and available literature data [31], it was noted that PETG exhibited anisotropic properties, both for compression and tensile tests. A schematic of the specimens with dimensions is presented in Fig. 5.

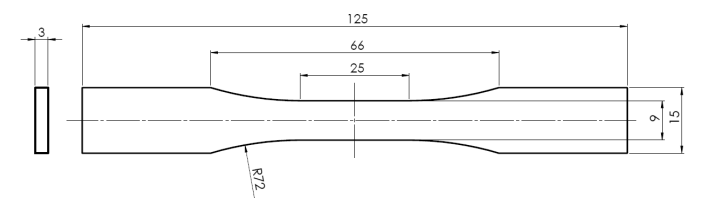


Fig. 5. Specimen dimensions for tensile tests according to ASTM D638-14 standard [43]

Figure 6 shows the true stress-true strain curves for the specimens manufactured in three printing directions. The curves from compression tests conducted by [31] were also included. The uniaxial tensile tests were performed using an MTS Criterion C45.105 universal testing machine at 22°C. The dog-bone specimens were investigated at a velocity of 5 mm/min. For each specimen building direction, four samples were prepared. It was observed that the printing direction affected the results obtained. For the XY printing direction, the elastic modulus, yield strength, and elongation are higher compared to the other two cases. The pronounced effect of the printing direction is visible for the curves obtained for YZ and 45° specimens. These groups of specimens demonstrated a smaller elastic modulus, yielded stress, and brittle fracture caused by delamination. The parameters of the specimens printed in these two directions are quite similar, with a small discrepancy between the elastic parts of the curves.

On the other hand, the curves taken from compression tests [31] are characterized by significantly smaller yield stress

compared to tensile specimens. Moreover, the brittle behavior of the specimens is more evident. The specimens manufactured along the 0X direction display a brittle fracture characteristic, which is similar to dog-bone specimens used for tensile tests conducted in this paper.

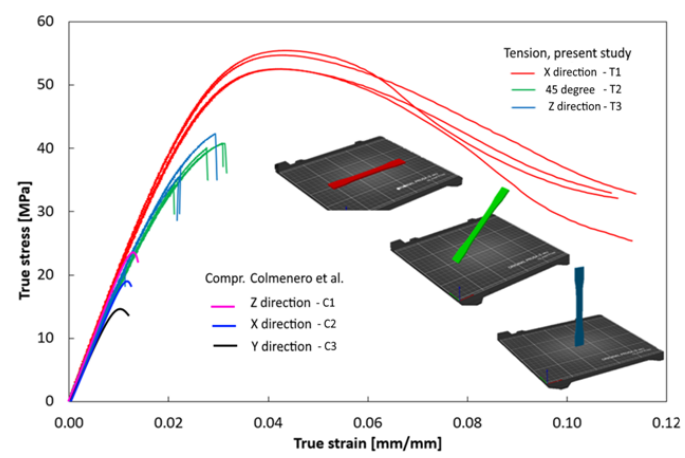


Fig. 6. True stress vs. true strain curves for PETG material obtained under different specimens and orientation of layers for printed specimens according to ASTM D638-14 standard [43] and compression test [31]

Since a strong anisotropy of the PETG and a pronounced effect of the printing direction were observed, which was previously reported by other scholars [20], the material properties of the selected constitutive model were determined based on these facts. The stress-strain curves obtained from the tests for each type of specimen (three in compression and tension) were averaged, and only one curve from each group was used for simulations. The results of uniaxial tensile and compression tests are summarized in Tables 3 and 4, respectively. The remaining material parameters were provided in the manufacturer's data sheet [35].

Table 3
Results of experimental studies of the PETG material obtained through the uniaxial tensile test conducted in this paper

Printing orientation	Tensile properties	S1	S2	S3	S4	Arithmetic average	Typical deviation
	Young's modulus [MPa]	2019.0	2034.0	2094.0	2094.0	2060.2	34.16
X direction (T1)	Yield strength [MPa]	40.5	41.0	42.0	41.8	41.3	0.61
	Fracture stress [MPa]	34.99	25.39	32.11	32.81	31.33	3.59
	Young's modulus [MPa]	1804.00	1795.00	1851.00	1800.00	1812.50	22.46
45 degree (T2)	Yield strength [MPa]	32.85	32.96	32.45	32.42	32.67	0.24
	Fracture stress [MPa]	29.61	36.11	34.95	37.11	34.45	2.89
	Young's modulus [MPa]	1885.00	1925.00	1929.00	1930.00	1917.25	18.71
Z direction (T3)	Yield strength [MPa]	35.01	33.42	n/d	31.65	33.36	1.37
	Fracture stress [MPa]	29.64	35.00	18.20	28.61	27.86	6.08

**Table 4**PETG data collected from the literature [31]

Printing orientation	Compression properties	S1	S2	S3	S4	S5	S6	Arithmetic average	Typical deviation
	Young's modulus [MPa]	1473.9	1207.1	1235.1	1244.6	1442.9	1373.4	1329.5	105.5
Z-axis (C1)	Yield strength [MPa]	21.7	22.7	22.7	22.9	22.8	22.3	22.5	0.4
	Fracture stress [MPa]	18.6	19.2	18.4	17.4	18.2	16.9	18.1	0.8
	Young's modulus [MPa]	704.8	1091.1	899.2	1537.8	1140.0	1334.7	1117.9	271.7
X-axis (C2)	Yield strength [MPa]	23.7	23.4	20.9	20.5	10.0	18.9	19.6	4.6
	Fracture stress [MPa]	23.1	22.8	21.5	20.7	9.5	19.3	19.5	4.6
	Young's modulus [MPa]	1504.3	937.7	1126.6	961.1	1254.4	959.94	1124.0	204.0
Y-axis (C3)	Yield strength [MPa]	12.3	16.0	14.3	11.5	12.7	17.1	14.0	2.0
	Fracture stress [MPa]	12.9	16.3	14.7	11.6	12.9	17.5	14.3	2.1

#### 3.2. Correlation of the constitutive model

Since there are no available constitutive models in the LS-Dyna library, considering the anisotropic properties and printing directions of the material, an elasto-viscoplastic constitutive (MAT\_PLASTICITY\_WITH\_DAMAGE - MPD) model was used instead to reproduce the behavior of the PETG material. Six different input curves and corresponding basic data were included based on the results shown in Section 3.1. Each model was named using the abbreviation "MPD" and the corresponding letter for building direction. For instance, MPD\_T1 represents the constitutive model with the properties determined based on the tensile tests for specimens printed in the 0X direction. Previously, this model was found to be effective for simulating the polymeric materials and the deformation process of cellular structures subjected to uniaxial compression tests [19, 44]. It is based on the Huber-Mises-Hencky (HMH) yield criterion in which deviatoric stresses  $S_{ij}$  satisfy the yield function  $\sigma_y$  as follows [45]:

$$\phi = \frac{1}{2} S_{ij} S_{ij} - \frac{\sigma_y^2}{3} \le 0, \tag{2}$$

$$\sigma_{y} = \beta \left[ \sigma_{0} + f_{h} \left( \varepsilon_{\text{eff}}^{p} \right) \right],$$
 (3)

where  $arepsilon_{arepsilon ff}^{p}$  is an effective plastic strain defined as

$$\varepsilon_{\text{eff}}^{p} = \int_{0}^{t} d\varepsilon_{\varepsilon ff}^{p}.$$
 (4)

 $\beta$  is a strain rate effect parameter (omitted in the present studies), and  $f_h$  is the hardening function, which can be specified in tabular form. However,  $f_h$  is usually defined as a linear function

$$f_h\left(\varepsilon_{\text{eff}}^p\right) = E_p\left(\varepsilon_{\text{eff}}^p\right),$$
 (5)

where  $E_p$  is the plastic hardening modulus.

The selected constitutive model was correlated based on the uniaxial tensile tests and compression tests conducted by other scholars, which were discussed in Section 3.1. Numerical simulations were performed using an implicit massively parallel processing (MPP) LS-Dyna solver. A discrete model of the specimens was developed using a hexagonal finite element, with an average size of the FEs corresponding to the optimum mesh size used for the modeling of the BCC structure. The basic data, such as yield stress and Elastic modulus, were determined based on the experimental data for each printing direction, whereas density and Poisson's ratio were imported from the manufacturer's data sheet [35] (Table 5). The MPD model requires effective stress (ES) vs. effective plastic strain (EPS) curve input based on the experimental tests (Table 6). Moreover, the damage (softening) curve was also adopted (Table 7). However, it was mainly applied in the numerical simulations of the BCC compression structures to allow elements to remain in the model without early numerical erosion and to maintain the continuity of the material.

Table 5

Mechanical properties of PETG used in the MPD model for compression and tension for three different printing directions

Model	Density, $\rho^b$ [kg/m <sup>3</sup> ]	Elastic modulus <sup>a</sup> E [MPa]	Poisson's ratio, v <sup>b</sup> [-]	Yield stress $^a$ , $R_e$ [MPa]
MPD_T1		2060.0		41.3
MPD_T2		1812.0		32.7
MPD_T3	1270.0	1917.0	0.39	33.3
MPD_C1		1329.0	0.07	22.5
MPD_C2		1117.0		19.6
MPD_C3		1124.0		14.0

<sup>&</sup>lt;sup>a</sup> from experiments (Section 3.1)

b from manufacturer [35]

Moreover, the assumption was that the damage curve does not change the stiffness of the material. Eventually, the points of this curve were determined iteratively.

**Table 6**Points of the es-eps curve of PETG used in the MPD model for compression and tension for three different printing directions

Tension						
Point	MP	D_T1	MP	D_T2	MP	D_T3
no.	EPS [%]	ES [MPa]	EPS [%]	ES [MPa]	EPS [%]	ES [MPa]
1	0.00	40.98	0.00	30.74	0.00	30.05
2	0.20	43.76	0.16	32.82	0.10	31.05
3	0.30	44.91	0.24	33.68	0.12	31.33
4	0.40	45.95	0.33	34.46	0.15	31.62
5	0.50	46.94	0.43	35.21	0.18	31.90
6	0.60	47.50	0.47	35.63	0.21	32.19
7	0.70	48.00	0.52	36.00	0.26	32.68
8	0.80	48.30	0.56	36.23	0.27	32.77
9	0.90	48.60	0.57	36.45	0.32	33.14
10	1.00	48.70	0.59	36.49	0.35	33.16
		C	ompressi	ion		
Point	MP	D_C1	MP	D_C2	O_C2 MPD_C3	
no.	EPS [%]	ES [MPa]	EPS [%]	ES [MPa]	EPS [%]	ES [MPa]
1	0.00	22.50	0.00	19.62	0.00	14.20
2	0.02	22.60	0.02	19.97	0.02	14.62
3	0.05	22.72	0.04	20.14	0.04	14.89
4	0.08	22.81	0.06	20.36	0.06	15.08
5	0.12	22.92	0.08	20.52	0.08	15.20
6	0.15	23.01	0.10	20.70	0.10	15.30
7	0.17	23.04	0.12	20.82	0.12	15.35
8	0.20	23.07	0.15	20.91	0.15	15.38
9	0.22	23.10	0.17	20.96	0.17	15.40
10	0.25	23.12	0.20	21.00	0.20	15.43

Table 7
Points of the damage curves of PETG used in the MPD constitutive model

Point no.	Eff. plastic strain [%]	Damage [-]
1	0.00	0.00
2	4.00	0.20
3	60.0	1.00

In Fig. 7, the true stress vs. true strain obtained based on the experimental tests and FEA are presented. The selected material provided an excellent correspondence with the laboratory data curves in both elastic and plastic ranges, indicating the correctness of the adopted material parameters for the model. It should be noted that the failure simulated using erosion was not considered in the model.

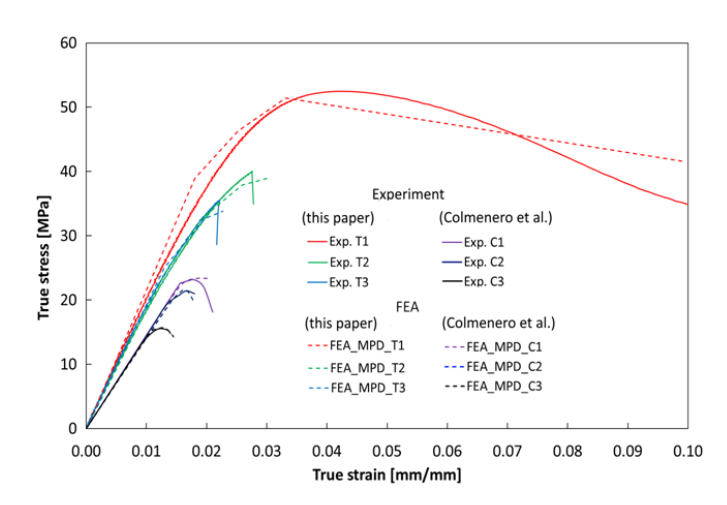


**Fig. 7.** Correlation in the constitutive model based on true stress-true strain obtained from experiment and FEA

## 4. UNIAXIAL COMPRESSION TESTS OF BCC 3D PRINTED TOPOLOGIES

#### 4.1. Experimental set-up

To properly evaluate the material response and structural behavior, the uniaxial compression tests of the BCC lattice structures and cubical specimens were conducted with three loading velocities: 0.17 mm/s, 1.0 mm/s, and 10.0 mm/s on the MTS Criterion Model 45 strength machine (Fig. 8). It was decided to compress the structures until they reached 70% of their height. After this point, the densification was observed to occur with a sudden increase in force on the force-displacement plot. The Canon EOS R camera with AF Micro-Nikkor 200 mm f/4D IF-ED lens was used to record the deformation process.

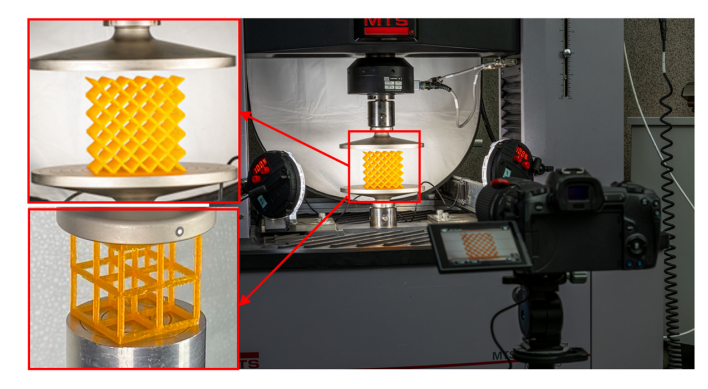


**Fig. 8.** Universal strength machine with recording system and closeup view of the tested BBC structures and one of the cubical specimens

#### 4.2. Numerical modeling

The correlated constitutive model of PETG material allowed us to perform the compression test of the BCC lattice structure using computer simulations. The validation of the model based on the experimental tests described earlier was followed by a comparison of the EA capabilities of three different strut cross sections: hexagonal, round, and square. Two types of elements were used to represent the structures: 1D beam elements (Hughes-Liu with cross section integration) and 3D hexagonal elements with eight nodes and one integration point. Furthermore, for a square cross section, mesh sensitivity studies were conducted to assess the influence of the mesh on the outcomes (Fig. 12). Two rigid surfaces were used to compress the BCC lattice structure: one was fixed, while for the second, a prescribed velocity was adopted based on the formula [8]

$$v(t) = \frac{\pi}{\pi - 2} \frac{S_{\text{max}}}{T} \left[ 1 - \cos\left(\frac{\pi}{2T}t\right) \right],\tag{6}$$

where  $S_{\text{max}}$  – final displacement of the rigid plate.

For each contact pair, i.e., rigid surface-lattice structure and self-contact of the lattice structure, a penalty-based contact with the Coulomb formulation was used. The friction was determined based on the trial-and-error approach, and the literature data with the value of FS=0.4 resulted in the best correlation with the experimental data. To reduce the model and save computation time, two symmetrical surfaces were adopted in the model, with ultimately a 1/4 of the model used in the simulations. A representative numerical model with appropriate initial boundary conditions is presented in Fig. 9.

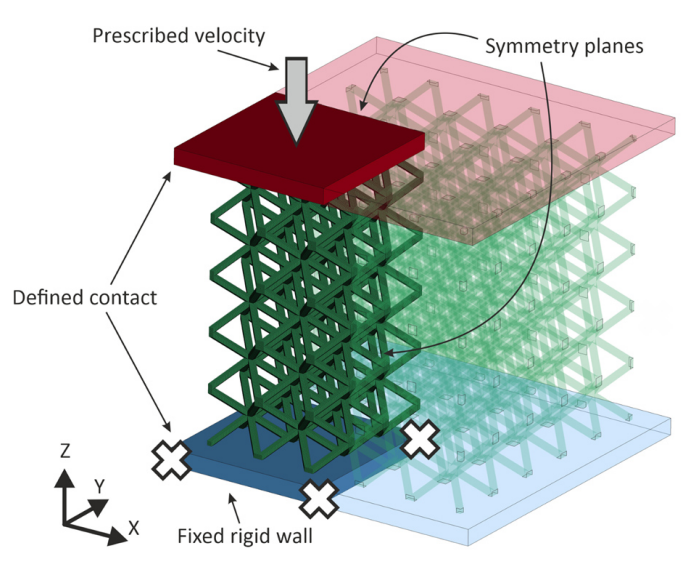


**Fig. 9.** Numerical model of lattice structure with highlighted initial-boundary conditions

#### 5. RESULTS AND DISCUSSION

### 5.1. Experimental results of the BCC compression tests

In Fig. 10, the deformation force plots are presented for all tested loading conditions. For each velocity, three specimens were used, and nine force vs. displacement curves are shown and

compared in the end. Even though different compression velocities were used, the initial slopes of the curves are nearly identical. For the two smaller velocities (0.17 mm/s and 1.0 mm/s), a plateau region was observed without any significant fluctuations in the deformation force plot. In contrast, a compression velocity of 10.0 mm/s resulted in a different characteristic compared to the other two cases. An instant drop in the force after the first peak was obtained, followed by visible drops and an increase in the force. This indicated that the failure mechanism changed from plastic deformation to brittle (Fig. 11), which demonstrates a strong strain-rate dependency on the printed PETG material. It should be noted that the present paper is mainly focused on quasi-static compression, and no simulations regarding dynamic loading were considered. Moreover, the authors did not conduct uniaxial tensile and/or compression tests for the material specimen at various deformation velocities. However, this issue needs to be considered while simulating the dynamic behavior of the PETG material, which has been previously demonstrated [20, 41, 42, 46].

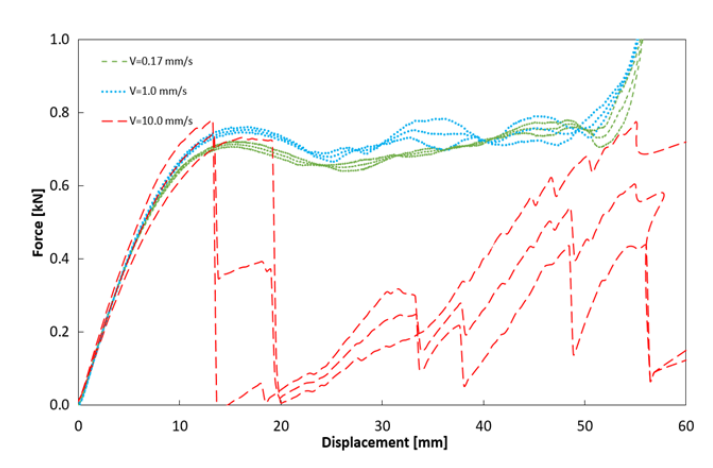
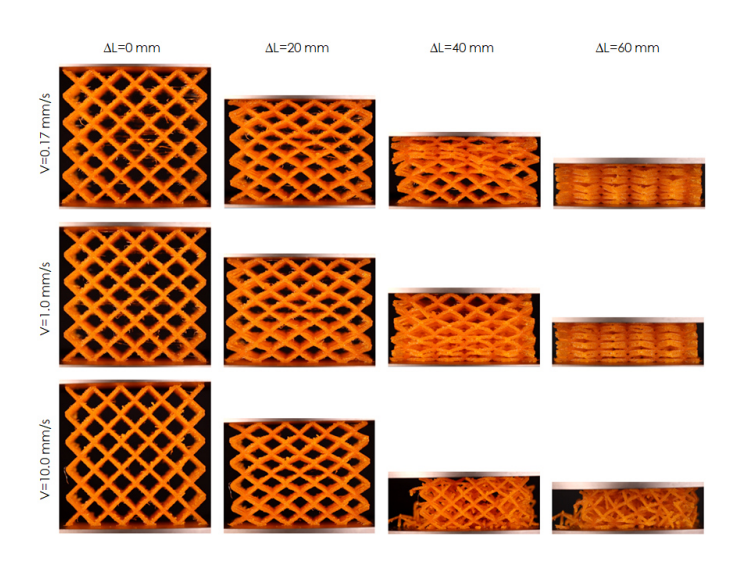


Fig. 10. Force vs. displacement from the experiment test



**Fig. 11.** Deformation process of the BCC lattice structures for three velocities and four selected time frames

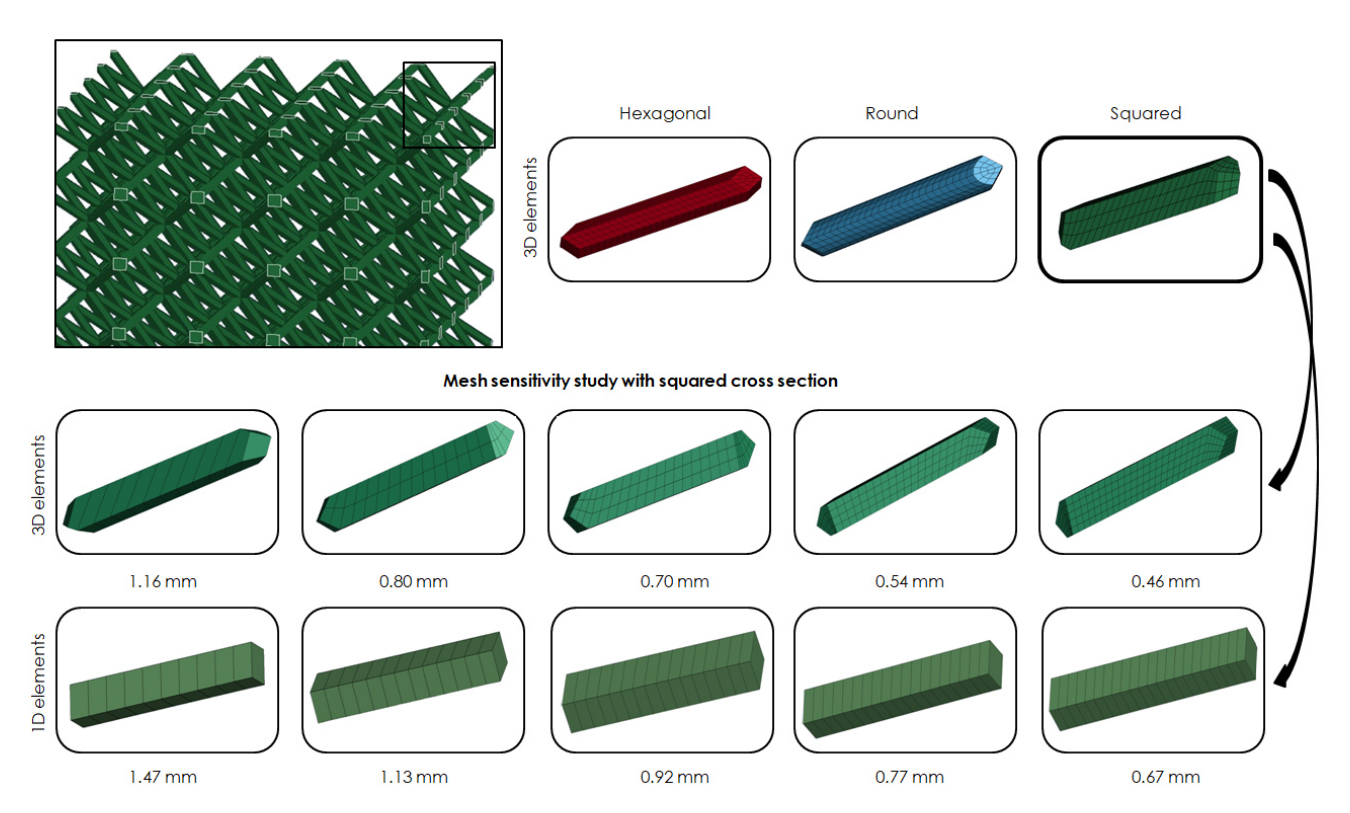


Fig. 12. Discrete BCC structure unit cell models using 1D and 3D types of finite elements

#### 5.2. Mesh sensitivity study

The first stage of numerical simulations was related to mesh sensitivity studies for a square beam cross section. Elements of the 1D beam (Hughes-Liu with cross section integration) and 3D hexagonal with eight nodes and one integration point were used. For each type of element, five different mesh sizes were prepared to select the optimal density and type of element (Table 8). Based on the results, absorbed energy, specific energy absorption (SEA), average force, and simulation time were compared. In this stage, the MPD model with the MPD\_C1 data was used. The numerical model was prepared according to Fig. 9. In Fig. 13 and Fig. 14, the deformation force vs. displacement plots are presented for brick and beam elements, respectively. The use of one 3D FE on a single strut thickness

**Table 8**Different element types and sizes in FEA approach for a square cross section

В	Brick	Beam		
Element size [mm]	No. of elements [–]	Element size [mm]	No. of elements [–]	
1.16	3 250	1.47	2500	
0.80	19 000	1.13	3250	
0.70	56 250	0.92	4000	
0.54	124 000	0.77	4750	
0.46	231 250	0.67	5500	

of 1.16 mm significantly reduces the stiffness of the structure, whereas for the model with two elements through strut thickness (FE size equal to 0.80 mm), a slightly smaller stiffness was obtained compared to the other three cases. For these remaining element sizes, the obtained curves are remarkably similar. In the case of 1D element modeling, regardless of the number of elements used on the strut thickness (from 10 to 22), the obtained results were almost identical (Fig. 14). In both cases, the obtained curves were compared with the experimental measurement. The most comparable results in terms of the overall shape of the force characteristics compared to the experiment were obtained for 3D brick FEs. On the contrary, for the models discretized using 1D beam elements, an ascending character of

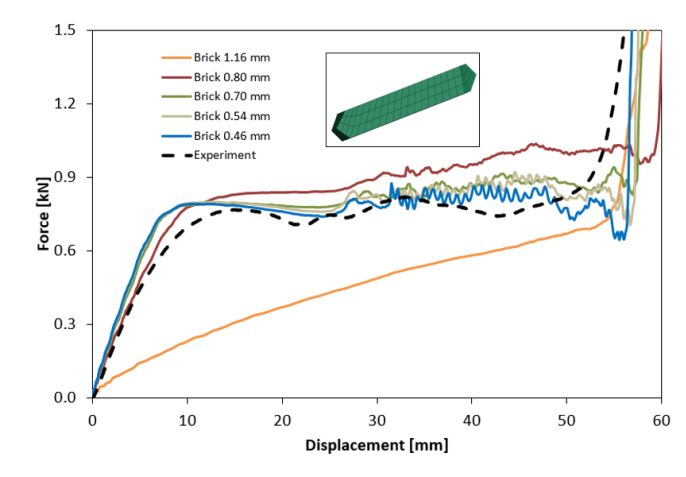


Fig. 13. Deformation force vs. displacement curves for the square cross section of the BCC lattice modeled using brick elements

the curve was observed without a visible plateau region seen both in experimental and numerical results using 3D elements. For both modeling approaches, the deformation force values are greatly overestimated, which resulted from the 3D printing method (detailed discussion is included in Section 5.3).

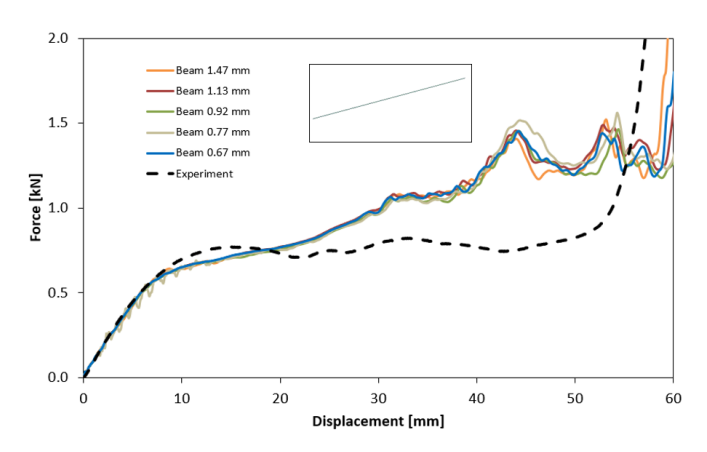


Fig. 14. Deformation force vs. displacement curves for the square cross section of the BCC lattice modeled using beam elements

For a more detailed analysis, the results of the mesh parametric study are collated in Table 9. All simulations were conducted using a 48-core computational cluster and an explicit MPP LS-Dyna code. For the final simulations presented in Section 5.3, the numerical model with three 3D elements across the strut thickness (size of 0.70 mm) was used. It should be mentioned that authors dealing with the subject of numerical modeling of BCC structures usually use 3D tetrahedral finite elements [25, 47]. The use of tetrahedral finite elements may be associated with larger numerical errors, especially when complex deformation exists, which is why the authors decided to use hexahedral elements in this study.

 Table 9

 Comparison of the two implemented methods of modeling

Element size [mm]	EA [J]	SEA [J/g]	Average force [kN]	Simulation time [min]
		Brick eler	nents	
1.16	30.50	0.63	0.44	0.27
0.80	51.00	1.05	0.88	1.12
0.70	52.50	1.08	0.82	3.73
0.54	53.20	1.10	0.81	11.40
0.46	52.50	1.08	0.77	28.20
		Beam eler	nents	
1.47	57.70	1.19	0.92	0.75
1.13	57.60	1.19	0.93	1.17
0.92	55.90	1.15	0.92	1.75
0.77	57.10	1.18	0.93	2.47
0.67	57.30	1.18	0.93	3.62

## 5.3. Numerical results of the BCC and cubic specimen compression tests

The uniaxial compression test of the BCC structure was simulated using the 3D brick elements with a size of 0.70 mm, which was selected based on the conducted mesh parametric study. Moreover, the hexagonal cross section according to the scheme shown in Fig. 9 was used, corresponding to the actual BCC structure.

In Fig. 15, the numerical deformation force histories are compared with experimental results. The numerical data are shown for the MPD model with parameters determined for three 3D printing directions, both in compression and tension (see Section 3.2). The FEA curves obtained for the MPD model with parameters determined from uniaxial tensile tests greatly overestimated the experimental outcome. The average value of the force from the FEA is 1.41 kN for MPD\_T1, 1.47 kN for MPD\_T2, and 1.20 kN for MPD\_T3, respectively, which is higher than the experimental value. On the other hand, the numerical model reproduced very well the experimental results for the constitutive parameters, which were based on the compression data from [31]. The best agreement between experiment and FEA was obtained for the MPD model with MPD\_C2 data. A strong anisotropy of the 3D printed PETG is clearly visible, and these findings are similar to previous papers [31,48,49]. The obtained results for the simulations and experiment using SEA, average force, and relative error are collated in Table 10. The presented

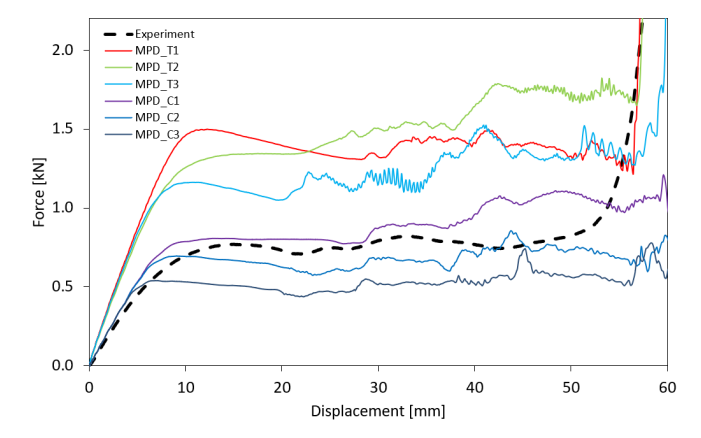


**Fig. 15.** Deformation force vs. displacement curves from experimental test and simulations

**Table 10**Result of the compression test for BCC topology

MPD	SEA [J/g]	Error [%]	Average force [kN]	Relative error [%]
MPD_T1	1.33	54.65	1.41	85.53
MPD_T2	1.89	119.77	1.47	93.42
MPD_T3	1.47	70.93	1.20	57.89
MPD_C1	1.05	22.09	0.87	14.47
MPD_C2	0.80	6.98	0.67	11.84
MPD_C3	0.64	25.58	0.52	31.58
EXP.	0.86	_	0.76	_

results clearly indicate the need to consider a strong anisotropy and printing orientation while simulating the structures manufactured via the FFF method and using PETG filament.

The deformation patterns of BCC topology obtained from FEA were compared with real-world observations presented in Fig. 16, where the selected stages of the BCC compression process with corresponding screenshots from the camera are shown. Additionally, to analyze the influence of different strut cross-sections, additional numerical studies were conducted with round and square cross-sections, while maintaining the same relative density (about 0.07). The boundary conditions of the model were the same in all cases (Fig. 9). Excellent reproduction of the structure deformation characteristics was observed for all types of cross-sections. Moreover, the typical behavior of BCC is visible: starting from the  $\Delta L = 20$  mm, the deformation pattern formed an X-shape and the shearing plane passed from the specimen corners in the vicinity of the rigid wall towards the center of the specimen, until the full densification. These observations are in agreement with the other papers [2, 3].

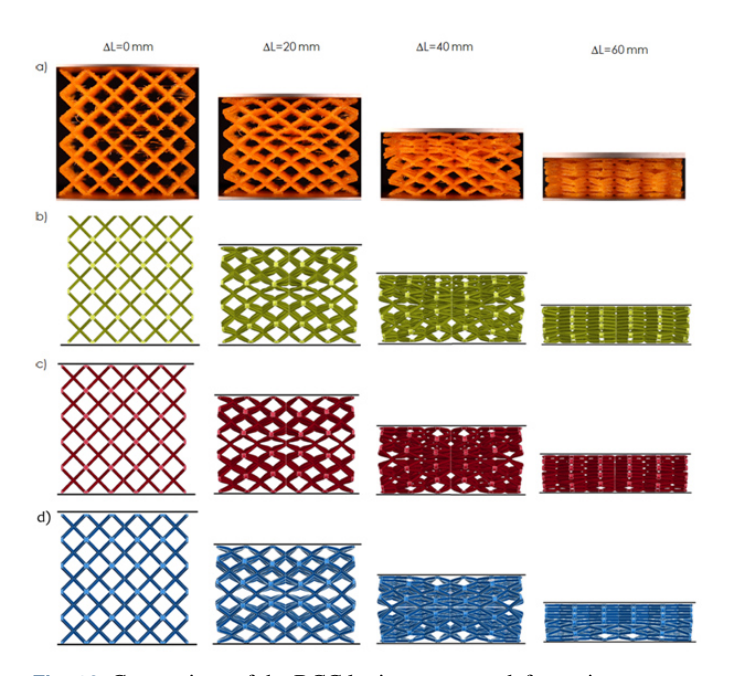


**Fig. 16.** Comparison of the BCC lattice structure deformation process: a) experimental tests and FEA with three different crosssections for the struts: b) hexagonal, c) round, and d) square

The deformation force plots obtained for the BCC model with the three types of cross-sections are compared with the experimental data in Fig. 17. For all three cases, the MPD\_C2 model was used; however, slight differences were observed for the initial slope of the curves. Furthermore, the model with a hexagonal cross section has the largest deformation force values, whereas the smallest were obtained for the square cross-section. This was reflected in the value of the absorbed energy: a summary of the results with different cross-sections is shown in Table 11.

To analyze more deeply the anisotropy properties of the PETG, additional tests were conducted based on the smaller cubical specimens described in Sections 2.1 and 2.3. In Fig. 18 and Fig. 19, deformation force vs. displacement curves are shown

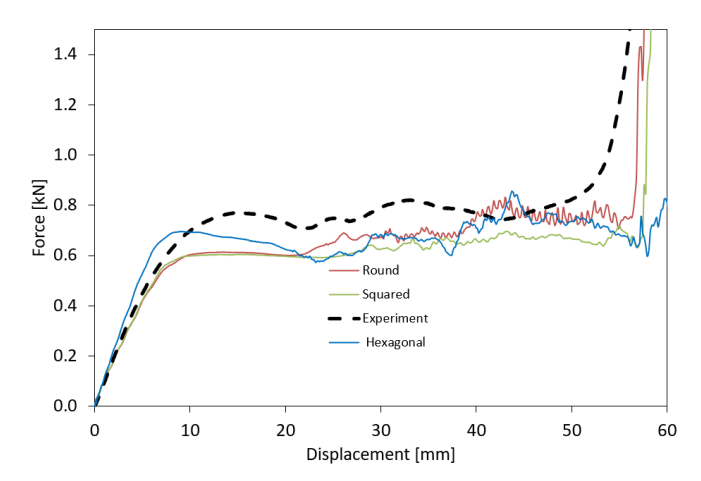


Fig. 17. Deformation force vs. displacement curves for the three cross-sections of the BCC lattice

 Table 11

 Comparison of the three cross-sections of the strut

Cross-section	SEA [J/g]	Error [%]	Average force [kN]	Relative error [%]
Hexagonal*	0.80	6.98	0.67	11.84
Round	0.78	9.30	0.66	13.16
Square	0.73	15.12	0.62	18.42
Experiment	0.86	0.00	0.76	-

<sup>\*</sup> Identical to experimental tests

for the BCCs and SQ specimens, respectively. These two types of specimens were 3D printed separately, with both compressed in two different directions to investigate the influence of the FFF building direction on the material response. Different values of deformation forces were obtained for both samples depending on the direction of compression loading. However, larger differences were observed for the SQ topology, in which struts were perpendicularly arranged to each other and the 3D printed layers were parallelly placed on each strut. This demonstrated the influence of the 3D printing process on the obtained material

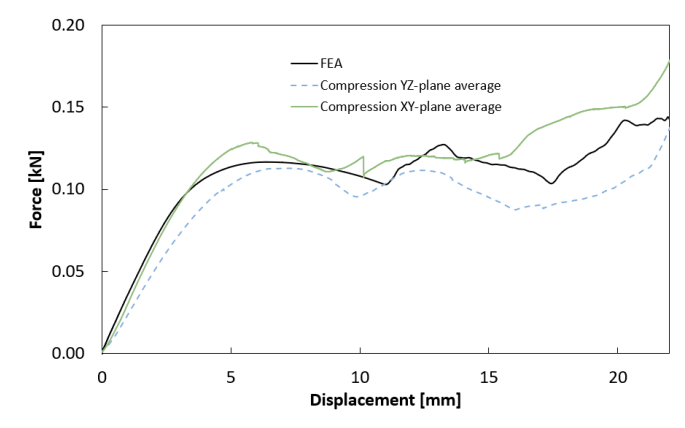


Fig. 18. Deformation force vs. displacement curves for elementary cells of BCC lattice structure

properties. Moreover, the deformation force histories obtained for FEA using the MPD model with tensile properties are also significantly higher compared to the experimental outcomes. On the contrary, a strong correlation between the results can be seen for the MPD model with compression data. This indicates that even in the case of testing the specimens made of single elementary cells, a strong influence of the printing direction was obtained.

A very good reproduction of the BCC topology with the modified MPD constitutive model was also confirmed in the BCC\_S and SQ specimens deformations presented in Fig. 20. In both

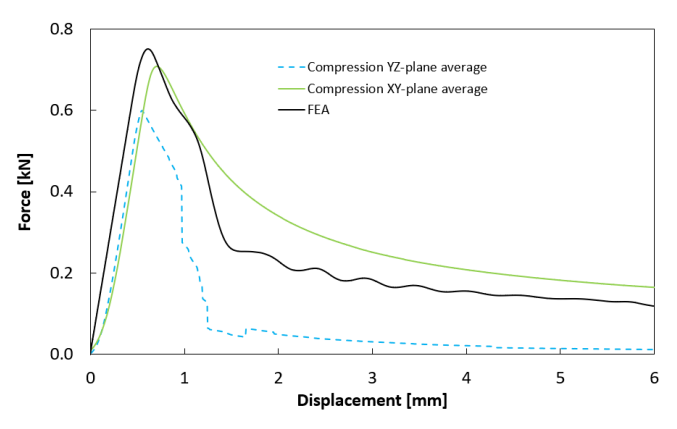


Fig. 19. Deformation force vs. displacement curves for SQ lattice structure

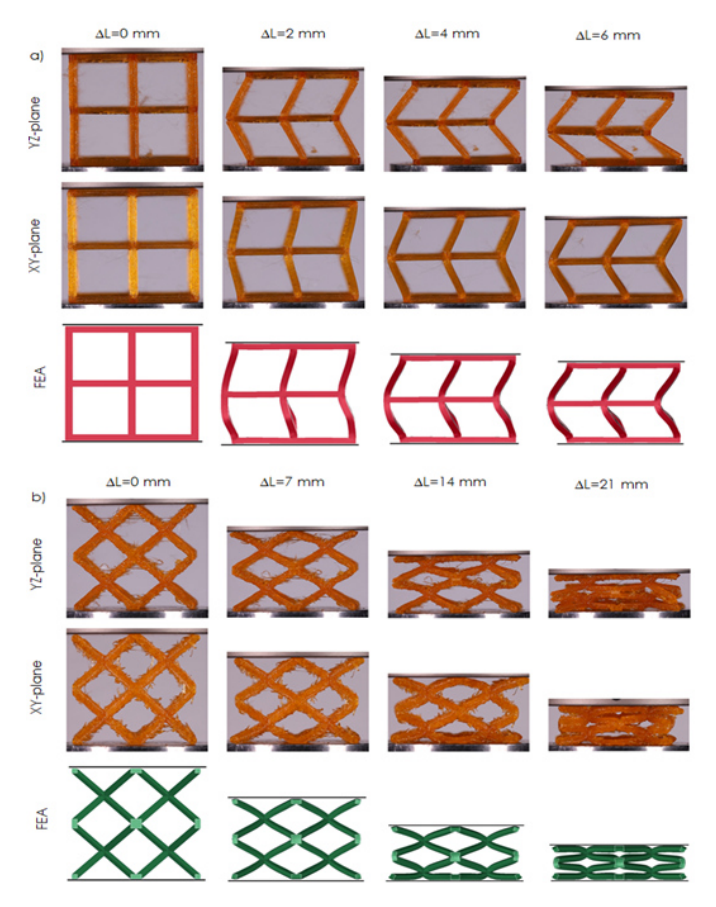


Fig. 20. Deformation comparison of: a) SQ, b) BCC\_s specimens

cases, the numerical model reflects the behavior of specimens satisfactorily; however, the influence of 3D printing and loading direction is noticeable. In FEA, an isotropic constitutive model was adopted, whereas the anisotropic properties of the PETG material had a pronounced effect on the specimen behavior demonstrated in the given outcomes.

#### 6. CONCLUSIONS

In the paper, the numerical and experimental results of the lattice BCC structures deformation process were presented. Based on the results, the following conclusions were drawn:

- The results obtained from the quasi-static tensile and compression tests proved a strong PETG anisotropy and the influence of the building direction on the material properties (Table 3 and Table 4).
- A strong strain-rate sensitivity was observed for the 3D printed PETG material while increasing the velocity during the test of uniaxial compression of BCC: the larger the velocity, the more brittle the fracture was (Fig. 11).
- The choice of the type of finite element and its size affects the results obtained and the calculation time (Table 9). In the case of brick elements, increasing the number of elements per strut thickness resulted in a change in the stiffness of the structure with a simultaneous increase in the computation time. The brick elements with a mesh size of 0.7 mm were found to be most optimal, considering the simulation time and accuracy.
- There are no available constitutive models in the LS-Dyna library that account for printing direction and anisotropy; therefore, the elasto-viscoplastic model was selected, and properties were determined based on the uniaxial tensile tests for the specimens printed in three directions. Additionally, compressive data from the literature were added, and the constitutive properties were also determined. Eventually, the best agreement with the experimental results was obtained for the curve from the uniaxial compression test MPD\_C2 (Fig. 15)
- Changing the type of strut cross section while maintaining the same relative density affects the EA properties of the BCC structure. In the analyzed case, the best absorption properties were obtained for the BCC modelled using struts with the hexagonal cross section (Fig. 17 and Table 11).

In future studies, other cellular and lattice structures will be studied, which will be manufactured using a metallic powder. Additionally, blast and ballistic tests will be simulated to assess the efficiency of such structures in extreme loading conditions.

#### **DATA AVAILABILITY**

The datasets used and/or analyzed during the current study are available from the corresponding author on reasonable request.

#### **ACKNOWLEDGEMENTS**

This research was supported by the Interdisciplinary Centre for Mathematical and Computational Modelling at the University of Warsaw (ICM UW) under computational grant no. GB84-20,

as well as with the support of the ANSYS National License coordinated by the Interdisciplinary Centre for Mathematical and Computational Modelling, University of Warsaw (ICM UW). Moreover, the article was co-financed from the state budget of Poland and awarded by the Minister of Science within the framework of the Excellent Science II Programme. This support is gratefully acknowledged. The numerical models were prepared using Altair HyperMesh software.

#### **REFERENCES**

- [1] T. Maconachie *et al.*, "SLM lattice structures: Properties, performance, applications and challenges," *Mater. Des.*, vol. 183, p. 108137, 2019, doi: 10.1016/j.matdes.2019.108137.
- [2] P. Li, Z. Wang, N. Petrinic, and C.R. Siviour, "Deformation behaviour of stainless steel microlattice structures by selective laser melting," *Mater. Sci. Eng. A.*, vol. 614, pp. 116–121, 2014, doi: 10.1016/j.msea.2014.07.015.
- [3] U.A. Dar, H.H. Mian, M. Abid, A. Topa, M.Z. Sheikh, and M. Bilal, "Experimental and numerical investigation of compressive behavior of lattice structures manufactured through projection micro stereolithography," *Mater. Today Commun.*, vol. 25, p. 101563, 2020, doi: 10.1016/j.mtcomm.2020.101563.
- [4] M. Smith *et al.*, "The quasi-static and blast response of steel lattice structures," *J. Sandw. Struct. Mater.*, vol. 13, pp. 479–501, 2010, doi: 10.1177/1099636210388983.
- [5] K. Yang, J. Wang, L. Jia, G. Yang, H. Tang, and Y. Li, "Additive manufacturing of Ti-6Al-4V lattice structures with high structural integrity under large compressive deformation," *J. Mater. Sci. Technol.*, vol. 35, pp. 303–308, 2019, doi: 10.1016/j.jmst. 2018 10.029.
- [6] A. Mauko *et al.*, "Dynamic Deformation Behaviour of Chiral Auxetic Lattice sat Low and High Strain-Rates," *Metals*, vol. 11, p. 52, 2021, doi: 10.3390/met11010052.
- [7] M. Kucewicz, P. Baranowski, J. Małachowski, P. Płatek, M. Konarzewski, and M. Stankiewicz, "Modelling and testing of 3D printed cellular structures under quasi-static and dynamic conditions," *Thin-Walled Struct.*, vol. 145, p. 106385, 2019, doi: 10.1016/j.tws.2019.106385.
- [8] M. Kucewicz, P. Baranowski, J. Małachowski, A. Popławski, and P. Płatek, "Modelling, and characterization of 3D printed cellular structures," *Mater. Des.*, vol. 142, pp. 177–189, 2018, doi: 10.1016/j.matdes.2018.01.028.
- [9] F.A. Santosa *et al.*, "Low velocity impact response of 3D printed structures formed by cellular metamaterials and stiffening plates: PLA vs. PETg," *Compos. Struct.*, vol. 256, p. 113128, 2021, doi: 10.1016/j.compstruct.2020.113128.
- [10] A. Nazir, K. Mekonen, A. Kumar and J-Y. Jeng, "A state-of-the-art review on types, design, optimization, and additive manufacturing of cellular structures," *Int. J. Adv. Manuf. Technol.*, vol. 104, pp. 3489–3510, 2019, doi: 10.1007/s00170-019-04085-3.
- [11] H. Yin, W. Zhang, L. Zhu, F. Meng, J. Liu, and G. Wen, "Review on lattice structures for energy absorption properties," *Compos. Struct.*, vol. 304, p. 116397, 2023, doi: 10.1016/j.compstruct.2022.116397.
- [12] P. Siemiński and G. Budzik. Techniki przyrostowe. Druk 3D. Drukarki 3D. Warsaw, OWPW, 2015.
- [13] J. Tatarczak, Z. Krzysiak, W. Samociuk, Z. Kaliniewicz, and L. Krzywonos, "A review of the newest 3D printing technology

- for metal objects," *Mechanik*, vol. 90, pp. 612–614, 2017, doi: 10.17814/mechanik.2017.7.89.
- [14] L.E. Murr *et al.*, "Fabrication of metal and alloy components by additive manufacturing: examples of 3D materials science," *J. Mater. Res. Technol.*, vol. 1, pp. 42–54, 2012, doi: 10.1016/S2238-7854(12)70009-1.
- [15] S. Singh, G. Singh, C. Prakash, and S. Ramakrishna, "Current status and future directions of fused filament fabrication," *J. Manuf. Processes*, vol. 55, pp. 288–306, 2020, doi: 10.1016/j.jmapro.2020.04.049.
- [16] J.Ch. Yungwirth, D.D. Radford, M. Aronson and H.N.G. Wadley, "Experiment assessment of the ballistic response of composite pyramidal lattice truss structures," *Composites, Part B*, vol. 39, pp. 556–569, 2008, doi: 10.1016/j.compositesb.2007.02.029.
- [17] M.F. Ashby, "The properties of foams and lattices," *Phil. Trans. R. Soc. A*, vol. 364, pp. 15–30, 2005, doi: 10.1098/rsta.2005.1678.
- [18] P. Płatek, P. Baranowski, J. Janiszewski, and M. Kucewicz, "Problems of Deformation and Damage Studies of Additively Manufactured Regular Cellular Structures," *Handbook of Damage Mechanics*, vol. 2, pp. 1–33, 2020, doi: 10.1007/978-1-4614-8968-9\_65-1.
- [19] M. Majdak, P. Baranowski, and J. Małachowski, "Numerical studies of the energy absorption capacities and deformation mechanisms of 2D cellular topologies," *Arch. Civ. Mech. Eng.*, vol. 24, p. 111, 2024, doi: 10.1007/s43452-024-00926-5.
- [20] C. Waly, S. Schulnig, and F. Arbeiter, "Strain rate-dependent failure modes of material extrusion-based additively manufactured PETG: A study on crack deflection and penetration," *Theor. Appl. Fract. Mech.*, vol. 136, p. 104834, 2025, doi: 10.1016/ j.tafmec.2024.104834.
- [21] Ch. Pan, Y. Han, and J. Lu, "Design and Optimization of Lattice Structures: A Review," *Appl. Sci.*, vol. 10, no. 18, p. 6374, 2020, doi: 10.3390/app10186374.
- [22] C. Güdür, T. Türkoğlu, and İ. Eren, "Effect of Lattice Design and Process Parameters on the Properties of PLA, ABS AND PETG Polymers Produced by Fused Deposition Modelling," *J. Mater. Mechat. A*, vol. 4, pp. 561–570, 2023, doi: 10.55546/jmm.1357217.
- [23] J. Dash et al., "A hybrid continuum beam optimisation model: the virtual extensometer method for efficient optimisation of lattice materials," Prog. Addit. Manuf., vol. 10, pp. 2535–2557, 2024, doi: 10.1007/s40964-024-00766-y.
- [24] M. Helou, and S. Kara, "Design, analysis and manufacturing of lattice structures: an overview," *Int. J. Comput. Integr. Manuf.*, vol. 31, pp. 243–261, 2017, doi: 10.1080/0951192X. 2017.1407456.
- [25] L. Bai, Ch. Yi, X. Chen, Y. Sun, and J. Zhang, "Effective Design of the Graded Strut of BCC Lattice Structure for Improving Mechanical Properties," *Materials*, vol. 12, no. 13, p. 2192, 2019, doi: 10.3390/ma12132192.
- [26] A. Seharing, A.H. Azman and S.A. Abdullah, "A review on integration of lightweight gradient lattice structures in additive manufacturing parts," *Adv. Mech. Eng.*, vol. 12, pp. 1–21, 2020, doi: 10.1177/1687814020916951.
- [27] Ch. Y. Seek, Ch. K. Kok, Ch. H. Lim and K.W.A. Liew, "Novel Lattice Structure for Enhanced Crush Energy Absorption," *Int. J. Tech.*, vol. 13, no. 5, pp. 1139–1148, 2022, doi: 10.14716/ ijtech.v13i5.5829.
- [28] M.J. Prajapati, Ch. Bhat, A. Kumar, S. Verma, Ch. Shang-Lin, and J.Y. Jeng, "Supportless Lattice Structure for Additive Man-



- ufacturing of Functional Products and the Evaluation of Its Mechanical Property at Variable Strain Rates," *Materials*, vol. 15, no. 22, p. 7954, 2022, doi: 10.3390/ma15227954.
- [29] S. Natesan, A. Natesan, S.V. Rohith and R.R. Hariharan, "Effect of varying unit cell size on energy absorption behavior of additive manufactured TPMS PETG lattice structure," *Prog. Addit. Manuf.*, vol. 8, pp. 1379–1397, 2023, doi: 10.1007/s40964-023-00407-w.
- [30] I.M. Alarifi, "Mechanical properties and numerical simulation of FDM 3D printed PETG/carbon composite unit structures," *J. Mater. Res. Technol.*, vol. 23, pp. 656–669, 2023, doi: 10.1016/j.jmrt.2023.01.043.
- [31] J.M. Mercado-Colmenero, M.D. La Rubia García, E.M. García, M. Rodriguez-Santiago, and C. Martin-Doñate, "Experimental and Numerical Analysis for the Mechanical Characterization of PETG Polymers Manufactured with FDM Technology under Pure Uniaxial Compression Stress States for Architectural Applications," *Polymers*, vol. 12, no. 10, p. 2202, 2020, doi: 10.3390/polym12102202.
- [32] R. Kumaresan, S. Mahendran, K. Kumaran, S. Wan, H. Wan, and R. Mustafizur, "Fused deposition modeling: process, materials, parameters, properties, and applications," *Int. J. Adv. Manuf. Technol.*, vol. 120, pp. 1531–1570, 2022, doi: 10.1007/s00170-022-08860-7.
- [33] PETG Data Sheet, https://www.iemai3d.com/wp-content/up loads/2020/12/PETG\_TDS.pdf
- [34] PETG Data Sheet, https://devel.lulzbot.com/filament/Rigid\_Ink/PETG%20DATA%20SHEET.pdf
- [35] PETG Data Sheet, https://www.prusament.com/wp-content/up loads/2023/07/PETG\_V0\_ENG.pdf
- [36] PETG Data Sheet, https://www.devildesign.com/download/ PETG\_-\_karta\_produktu.pdf
- [37] M.H. Hsueh *et al.*, "Effect of Printing Parameters on the Thermal and Mechanical Properties of 3D-Printed PLA and PETG, Using Fused Deposition Modeling," *Polymers*, vol. 13, no. 11, p. 1758, 2021, doi: 10.3390/polym13111758.
- [38] K. Szykiedans, W. Credo, and D. Osiński, "Mechanical properties of PETG 3-D prints," *Procedia Eng.*, vol. 177, pp. 455–461, 2017, doi: 10.1016/j.proeng.2017.02.245.

- [39] B. Ergene and C. Bolat, "An experimental investigation on the effect of test speed on the tensile properties of the petg produced by additive manufacturing," *Inter. J. 3D Print. Technol. Digit. Ind.*, vol. 6, pp. 250–260, 2022, doi: 10.46519/ij3dptdi.1069544.
- [40] S. Valvez, A.P. Silva and P.N.B. Reis, "Compressive Behaviour of 3D-Printed PETG Composites," *Aerospace*, vol. 9, no. 3, p. 124, 2022, doi: 10.3390/aerospace9030124.
- [41] E.C.Y. Ching, R.K.Y Li and Y.-W. Mai, "Effects of gauge length and strain rate on fracture toughness of polyethylene terephthalate glycol (PETG) film using the Essential Work of Fracture analysis," *Polym. Eng. Sci.*, vol. 40, pp. 310–319, 2000, doi: 10.1002/pen.11164.
- [42] N. Vidakis, M. Petousis, E. Velidakis, M. Liebscher, V. Mechtcherine, and L. Tzounis, "On the Strain Rate Sensitivity of Fused Filament Fabrication (FFF) Processed PLA, ABS, PETG, PA6, and PP Thermoplastic Polymers," *Polymers*, vol. 12, p. 2924, 2020, doi: 10.3390/polym12122924.
- [43] ASTM D638-14, Standard Test Method for Tensile Properties of Plastics. ASTM International, West Conshohocken. PA, 2014.
- [44] M. Kucewicz, P. Baranowski, and J. Małachowski, "A method of failure modeling for 3D printed cellular structures," *Mater. Des.*, vol. 174, p. 107802, 2019, doi: 10.1016/j.matdes.2019.107802.
- [45] Hallquist J. LS-DYNA® theory manual. 2006.
- [46] M. Petousi *et al.*, "A Coherent Assessment of the Compressive Strain Rate Response of PC, PETG, PMMA, and TPU Thermoplastics in MEX Additive Manufacturing," *Polymers*, vol. 15, p. 3926, 2023, doi: 10.3390/polym15193926.
- [47] S.K. Shah, A. Sur, and M. Shah, "Performance prediction of different BCC lattice structures under static loading: an experimental approach," *J. Braz. Soc. Mech. Sci. Eng.*, vol. 45, p. 581, 2023, doi: 10.21203/rs.3.rs-2969347/v1.
- [48] D. Popescu; A. Zapciu, C.G. Amza, B. Florin, and R. Marinescu, "FDM process parameters influence over the mechanical properties of polymer specimens: A review," *Polym. Test.*, vol. 69, pp. 157–166, 2018, doi: 10.1016/j.polymertesting.2018.05.020.
- [49] J.R.C Dizon, A.H. Espera, Q. Chen and R.C. Advincula, "Mechanical characterization of 3D-printed polymers," *Addit. Manuf.*, vol. 20, pp. 44–67, 2018, doi: 10.1016/j.addma. 2017.12.002.